

Geochemistry, Geophysics, Geosystems

RESEARCH ARTICLE

10.1029/2018GC007536

Key Points:

- Autonomous underwater vehicle and submersible surveys carried out over inactive detachment fault on Mid-Atlantic Ridge
- Sediment thickness and volatile content of lavas were used to track tectonic activity
- Seafloor observations suggest that slip continued after a volcanic intrusion into detachment fault footwall

Supporting Information:

- Supporting Information S1

Correspondence to:

R. E. Parnell-Turner,
rparnellturner@ucsd.edu

Citation:

Parnell-Turner, R. E., Mittelstaedt, E., Kurz, M. D., Jones, M. R., Soule, S. A., Klein, F., Wanless, V. D., & Fornari, D. J. (2018). The final stages of slip and volcanism on an oceanic detachment fault at 13°48'N, Mid-Atlantic Ridge. *Geochemistry, Geophysics, Geosystems*, 19. <https://doi.org/10.1029/2018GC007536>

Received 21 MAR 2018

Accepted 20 JUL 2018

Accepted article online 18 AUG 2018

The Final Stages of Slip and Volcanism on an Oceanic Detachment Fault at 13°48'N, Mid-Atlantic Ridge

R. E. Parnell-Turner^{1,2} , E. Mittelstaedt³ , M. D. Kurz¹, M. R. Jones⁴ , S. A. Soule¹, F. Klein¹, V. D. Wanless⁵ , and D. J. Fornari¹

¹Woods Hole Oceanographic Institution, Woods Hole, MA, USA, ²Now at Institute of Geophysics and Planetary Physics, Scripps Institution of Oceanography, University of California, San Diego, CA, USA, ³Department of Geological Sciences, University of Idaho, Moscow, ID, USA, ⁴Massachusetts Institute of Technology/Woods Hole Oceanographic Institution Joint Program in Oceanography, Woods Hole, MA, USA, ⁵Department of Geosciences, Boise State University, Boise, ID, USA

Abstract While processes associated with initiation and maintenance of oceanic detachment faults are becoming better constrained, much less is known about the tectonic and magmatic conditions that lead to fault abandonment. Here we present results from near-bottom investigations using the submersible *Alvin* and autonomous underwater vehicle *Sentry* at a recently extinct detachment fault near 13°48'N, Mid-Atlantic Ridge, that allow documentation of the final stages of fault activity and magmatism. Seafloor imagery, sampling, and near-bottom magnetic data show that the detachment footwall is intersected by an ~850 m-wide volcanic outcrop including pillow lavas. Saturation pressures in these vesicular basalts, based on dissolved H₂O and CO₂, are less than their collection pressures, which could be explained by eruption at a shallower level than their present depth. Sub-bottom profiles reveal that sediment thickness, a loose proxy for seafloor age, is ~2 m greater on top of the volcanic terrain than on the footwall adjacent to the hanging-wall cutoff. This difference could be explained by current-driven erosion in the axial valley or by continued slip after volcanic emplacement, on either a newly formed or pre-existing fault. Since current speeds near the footwall are unlikely to be sufficient to cause significant erosion, we favor the hypothesis that detachment slip continued after the episode of magmatism, consistent with growing evidence that oceanic detachments can continue to slip despite hosting magmatic intrusions.

1. Introduction

Exhumation of deep crustal rocks in the footwall of large-offset normal faults called detachments, leading to the formation of structures termed core complexes, was first recognized in the continents (Coney, 1974; Coney & Harms, 1984; Lister & Davis, 1989). Domed bathymetric highs on slow- and ultraslow-spreading mid-ocean ridges were later identified as oceanic core complexes (OCCs), with similar dimensions, fault geometry, and exhumation to those in terrestrial settings (e.g., Dick, 1989; Karson & Dick, 1983; Tucholke & Lin, 1994). Now recognized along large portions of Atlantic, Indian, and Arctic Ocean spreading centers, oceanic detachment faults are commonly thought to exhume lower crustal and upper mantle rocks to the seafloor (Blackman et al., 1998; Cannat et al., 2006; Dick, 1989; Karson & Dick, 1983; Tucholke et al., 1998). Many domed OCCs have been documented at mid-ocean ridges and are often characterized by corrugations extending up to tens of kilometers parallel to the spreading direction, leading to the definition of a distinct mode of seafloor spreading (Escartín et al., 2008; Escartín & Canales, 2011; Ohara et al., 2001; Smith et al., 2006). OCC domes are spatially discrete features, consisting of a ridge-parallel breakaway zone formed when the fault initiated and a low-angle slip surface that extends toward the mid-ocean ridge axis (Blackman et al., 2009). The point at which the footwall emerges from the seafloor, called the hanging-wall cutoff (or termination), marks the most recently exposed portion of fault scarp near the spreading axis. The total spreading-parallel extent of exposed fault surface suggests that detachments can accommodate plate spreading on timescales of 1–2 Ma, reflecting cycles of initiation, maintenance, and cessation of slip (MacLeod et al., 2009; Okino et al., 2004; Tucholke et al., 1998). The final stages of this detachment fault cycle are poorly understood, with ongoing debate about whether slip ceases abruptly due to an increase in magmatism or can continue following the intrusion of magmatic bodies such as dikes and sills (Bonnemains et al., 2017).

Numerical models predict that the style of crustal accretion is sensitive to the fraction of plate separation accommodated by dike intrusion, and initiation and maintenance of OCCs may be driven by variations in magma supply

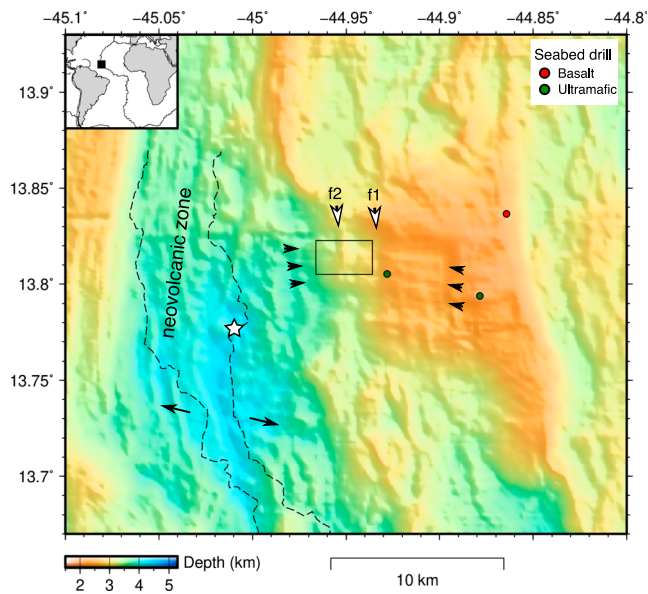


Figure 1. Bathymetry of Mid-Atlantic Ridge near 13°48'N oceanic core complex (Smith et al., 2006). Inset: Location of study site (black box) and plate boundaries (black lines). Main panel: Dashed line marks neovolcanic zone, interpretation from Mallows and Searle (2012) based on deep-tow sidescan sonar data; black box is *Sentry* dive 374; star is location of volatile-rich (“popping”) rocks recovered during cruise AT33-03; colored circles are samples acquired by seabed rock drill (MacLeod et al., 2009); large black arrows show plate spreading direction; small black arrow heads mark spreading-parallel corrugations; numbered white arrow heads show N-S trending faults crossing corrugated dome.

(Buck et al., 2005; Tian & Choi, 2016; Tucholke et al., 2008). Other models show that the rate of magma intrusion into the brittle lithosphere controls fault evolution, while dike injection into deeper layers only controls the lithology of exhumed material, meaning that OCC formation can be supported even when magma supply at deeper levels is high (Olive et al., 2010). Even where total magma supply is constant, focusing of melt by lateral dike propagation may influence the maintenance or cessation of slip on detachment faults (MacLeod et al., 2009), although this concept is yet to be quantitatively tested.

Here we document the final tectonic and magmatic events associated with the detachment fault system at 13°48'N on the Mid-Atlantic Ridge (MAR), which has recently become inactive (Figure 1). Previous studies have identified numerous OCCs along this segment of the MAR, with seafloor mapping and seismicity patterns suggesting that nearby detachment faults at 13°20'N and 13°30'N are presently, or were very recently, active (Craig & Parnell-Turner, 2017; Escartín et al., 2003; Parnell-Turner et al., 2017; Smith et al., 2003). We use detailed near-bottom bathymetric, magnetic, and compressed high-intensity radar pulse (CHIRP) sub-bottom data acquired by autonomous underwater vehicle (AUV) *Sentry* to map the exposed fault surface in detail. We analyze in situ samples collected by deep submergence vehicle *Alvin* and constrain the eruption pressure of basalts overlying the OCC using dissolved volatile concentrations (e.g., Dixon et al., 1988). These combined observations are used to assemble a coherent series of events surrounding the cessation of slip on this detachment fault.

1.1. Geological Setting and Prior Observations

The corrugated dome of the 13°48'N OCC is located east of the MAR axial valley and was first identified in shipboard multibeam bathymetric data (Figure 1; Smith et al., 2006, 2008). Low acoustic backscatter in towed sidescan sonar images acquired on top of the dome is consistent with a thick cover of sediment, interpreted to reflect fault inactivity (MacLeod et al., 2009; Mallows & Searle, 2012). Two north-south trending faults (f1 and f2, at 44.93°W and 44.95°W, respectively; Figure 1), which cut across the corrugated dome, have been previously identified based upon deep-towed sidescan sonar data (MacLeod et al., 2009; Mallows & Searle, 2012). Since corrugations continue westward beyond both of these faults, the hanging-wall cutoff is thought to lie to the west, closer to the axis (Mallows & Searle, 2012). Rock samples, acquired in situ using a seabed rock drill from the western part of the domed surface, are composed of hydrothermally altered peridotite, while basalt, diabase, and trondjemite were recovered from the eastern massif (MacLeod et al., 2009). These spatial observations and samples led MacLeod et al. (2009) to conclude that tectonic spreading ceased at the 13°48'N OCC in the past 0.4–0.9 Ma and has since been superseded by magmatic accretion at the ridge axis.

2. Methods

As part of a wider study of the occurrence of volatile-rich lavas on the MAR near 14°N during R/V *Atlantis* cruise AT33-03, the OCC at 13°48'N was surveyed in detail by *Sentry* during dive 374 and sampled during *Alvin* dive 4822 in March 2016.

2.1. Near-Bottom Geophysical Data

Sentry surveyed at 60–65 m above the seafloor at a speed of ~0.8–1.0 m/s, acquiring bathymetric data using a 400-kHz Reson 7125 multibeam sonar. These data were processed using MB-System software and gridded at 1 m node spacing (Figure 2a; Caress & Chayes, 1996).

Magnetic data were acquired using a set of three 3-axis digital fluxgate magnetometers carried by *Sentry*. These data were gridded at 50 m, upward continued to a uniform depth plane (2,500 m below sea level; Guspi, 1987) and inverted for crustal magnetization assuming a 100 m-thick source layer following the approach of Tivey et al. (1993); see supporting information for full methods. The final magnetization solution was obtained by applying an annihilator, which accounts for ambiguity in the inversion, and yields a positive

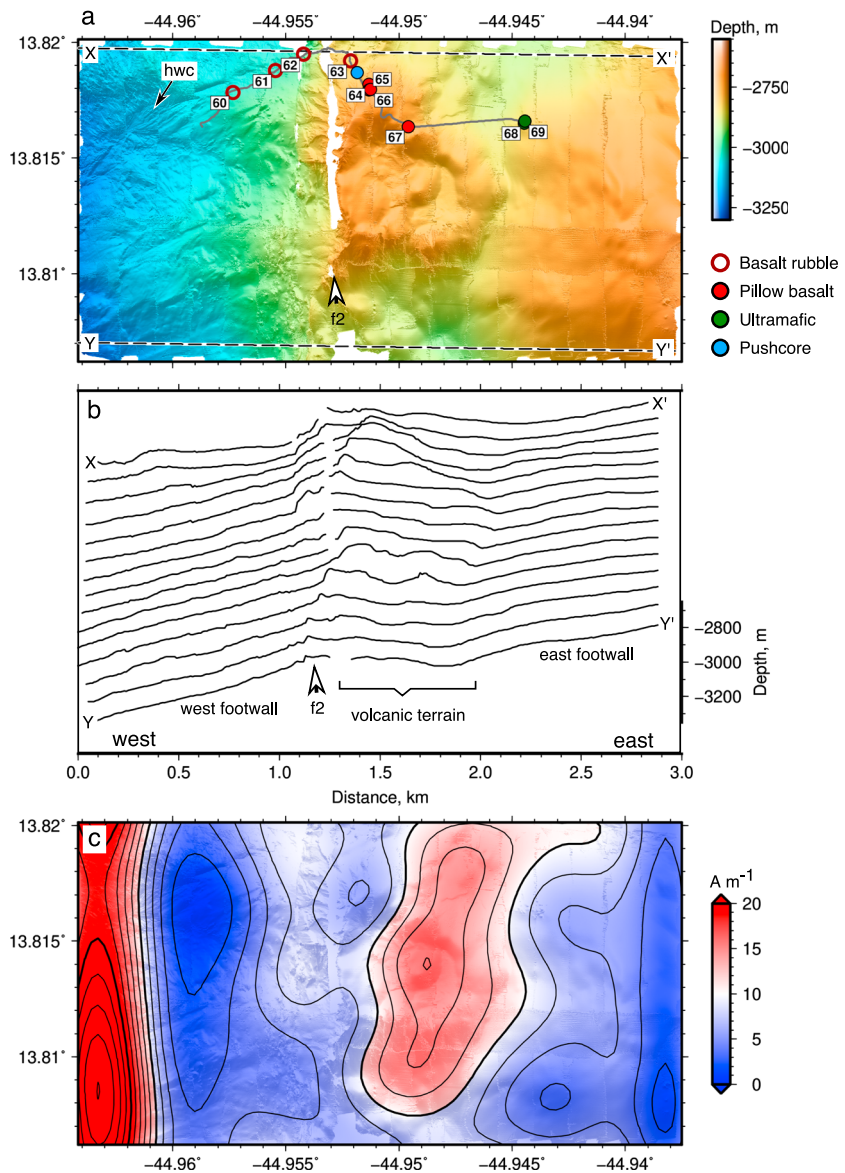


Figure 2. Near-bottom bathymetry and magnetization at 13°48'N oceanic core complex acquired by autonomous underwater vehicle *Sentry*. (a) Bathymetry, gridded at 1 m × 1 m cell size, illuminated from northwest. Gray line/colored dots are trackline/sampling sites from *Alvin* dive 4822, site numbers labeled without AL4822- prefix; dashed lines show location of profiles in (b); black arrow marks hanging-wall cutoff (hwc); white arrow marks fault scarp f2. (b) Bathymetric profiles. (c) Magnetization intensity.

magnetization since the crust is assumed to be <781 ka old, that is, formed after the Bruhnes-Matuyama reversal and thus is normally polarized (Figure 2c; Parker & Huestis, 1974).

Sidescan sonar data were acquired by *Sentry* using an Edgetech 2200M unit operating at dual frequencies of 120 and 410 kHz (Figure 3). CHIRP data were acquired simultaneously with sidescan data as part of the Edgetech system, with a frequency sweep of 4–24 kHz, yielding a vertical resolution of ~10 cm; lithology-dependent penetration is expected to be <10 m (Figure 4). CHIRP data were processed using MB-System and Seismic Unix software (Caress & Chayes, 1996; Cohen & Stockwell, 2013). Processing consisted of applying a zero-phase, sine-squared band-pass filter (frequencies 0.05, 0.1, 30, and 35 kHz) to remove noise from other instruments on the vehicle; time-dependent linear gain; trace balance; clipping of extreme trace values; and depth conversion using a constant (water) velocity of 1,500 m/s, following Parnell-Turner et al. (2014). The resulting SEG-Y format data were interpreted using OpendTect software.

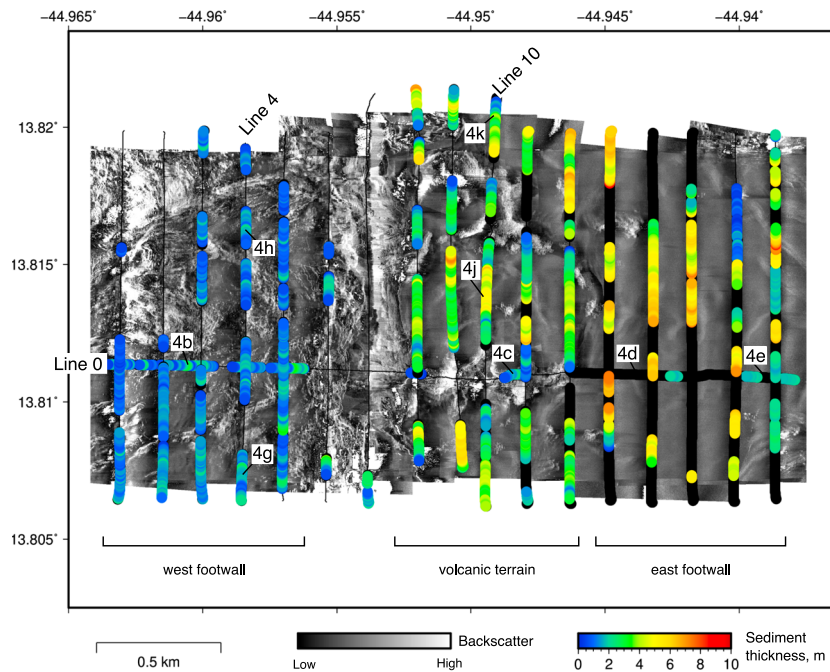


Figure 3. Sidescan sonar backscatter (gray shades) overlain with sediment thickness calculated from CHIRP profiles acquired during *Sentry* dive 374. Colored dots indicate spot sediment thickness estimates, spaced at ~ 1 m intervals along profiles; black dots indicate sediment of unknown thickness; labeled black lines are track lines, numbered boxes show location of zooms in Figure 4. Note the three distinct domains of sediment thickness, which increases from west to east.

2.2. Geological Sampling and Analysis

Ten in situ rock samples (AL4822-060 to AL4822-069), one push core, video and still photographic images were acquired during *Alvin* dive 4822 (track and sample locations are shown in Figure 2a). Major elements were analyzed at Boise State University using a Cameca SXFive electron microprobe (Table 1). Dissolved CO_2 and H_2O concentrations within quenched rinds of the recovered glassy basalt samples were measured using the Cameca 1280 secondary ion mass spectrometer at the Northeast National Ion Microprobe Facility at Woods Hole Oceanographic Institution, using methods based on Hauri et al. (2002); see supporting information for full methods and Table 1 for results. The presence or absence of vesicles was determined on $10\times$ magnification reflected-light photomicrographs of polished glass fragments from the outer quenched 1 cm of the lava samples (Figure 5h). The exsolved CO_2 content was measured at the Isotope Geochemistry Facility at Woods Hole Oceanographic Institution for samples AL4822-064 and AL4822-066 by capacitance manometry during in vacuo crushing of the glass chips.

3. Results

3.1. Near-Bottom Bathymetric Data

Near-bottom bathymetric data show the detailed terrain of the $13^\circ 48' \text{N}$ OCC (Figure 2a), which includes well-developed, curved, NW-SE trending hanging-wall cutoff that is clearly imaged near the western edge of the *Sentry* survey, marking the separation between the footwall and hanging wall of the detachment fault. East of the hanging-wall cutoff, the footwall rises upward with a slope of $\sim 15^\circ$ and is cut by a series of linear channel-like features that may result from local mass wasting (Figure 2a). Slumping and sliding are also evident from numerous rubble blocks and abundant talus on the seafloor recorded by *Alvin* dive video, and also the irregular sidescan sonar returns, with patches of high backscatter probably indicating loose rubble and scree (Figure 3a).

The scarp of fault f2 is located ~ 1 km east of the hanging-wall cutoff and caused navigational problems for *Sentry* (see data gaps at 44.953°W in Figure 2a). This scarp marks the western edge of a series of smooth,

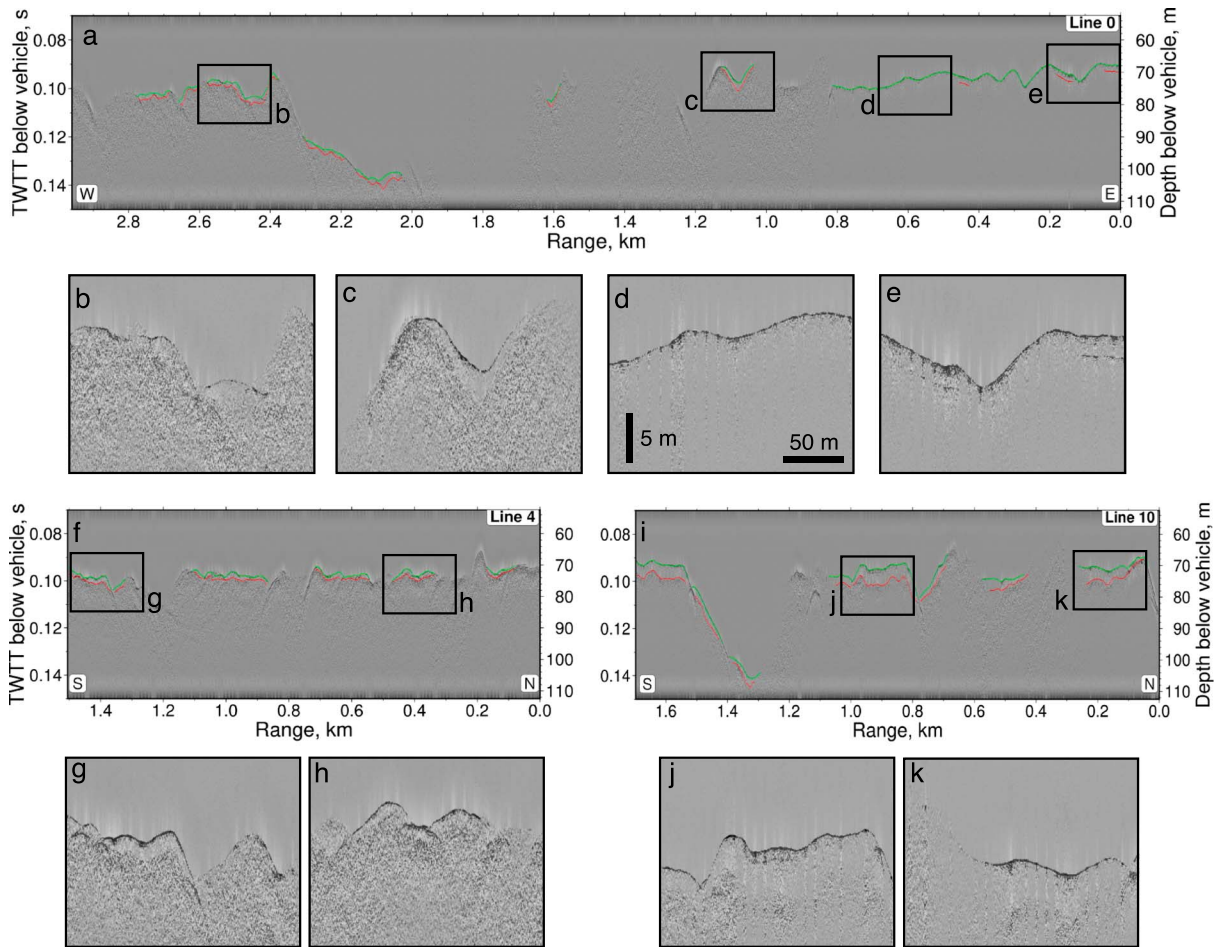


Figure 4. CHIRP profiles from *Sentry* dive 374, locations of profiles and zooms shown in Figure 3. Vertical axis plotted relative to vehicle, as two-way travel time (TWTT) and depth (assuming a velocity of 1,500 m/s). (a) Line 0. Green lines are seabed with sedimentary material beneath; red lines are sediment-basement interface where visible; boxes are zooms shown below. (b) Thin sediment on west footwall; (c) apparent sediment pond on edge of volcanic terrain; (d) highly reflective seabed with acoustically transparent subsurface on east footwall; (e) highly reflective seabed with weak basement reflection indicating ~3 m-thick sediment on east footwall. (f) Line 4. (g and h) Clearly imaged ~1-m-thick sediment on west footwall. (i) Line 10. (j and k) Weak basement reflections beneath highly reflective seabed show ~5 m thick sediment on volcanic terrain.

roughly equant domes typically 150–200 m in diameter, which coalesce to form a ~ 800 m-wide terrain with ~150 m relief, and a broad ring-shaped feature centered on 44.95°W, 13.813°N (Figure 2a). This series of domes corresponds to the N-S trending bathymetric high previously interpreted as a normal fault (MacLeod et al., 2009; Mallows & Searle, 2012). The circular bathymetric geometry (Figure 2a), high crustal magnetization (Figure 2c), and in situ pillow basalts (Figure 5a) demonstrate that at least the upper portion of this bathymetric high is volcanic in origin rather than tectonic as suggested by MacLeod et al. (2009) and Mallows and Searle (2012). Scalloped bathymetry (example at 13.812°N; Figure 2a) and the presence of mass-wasted debris on the slope to the west, from *Alvin* dive video and sidescan sonar backscatter imagery (Figure 3), support the interpretation that fault f2 has partly displaced the volcanic domes. These observations suggest that slop on the fault took place after volcanic emplacement. Bathymetric profiles over this terrain show that it has an overall eastward slope of ~10°, that is, likely back-tilted relative to the footwall dip (Figure 2b). East of this volcanic feature, the seafloor rises upward with a slope of ~16° and is remarkably smooth in comparison to seafloor between the hanging-wall cutoff and the volcanic cones. We interpret this area to represent a continuation of the detachment fault footwall, which extends ~10 km eastward toward the breakaway and is characterized by kilometer-scale corrugations (Figure 1).

Table 1
Major Element Compositions, Volatile Concentrations, and Saturation Pressures of Basaltic Samples Collected During Alvin Dive 4822

Sample	Lat. (N)	Lon. (W)	Depth (m)	Major element composition										Volatile concentration			Saturation pressure (MPa)	CO ₂ vesicles (ppm)
				SiO ₂ (wt%)	TiO ₂ (wt%)	Al ₂ O ₃ (wt%)	FeO (wt%)	MnO (wt%)	MgO (wt%)	CaO (wt%)	Na ₂ O (wt%)	K ₂ O (wt%)	P ₂ O ₅ (wt%)	Total (wt%)	CO ₂ (ppm)	H ₂ O (wt%)		
AL4822-064	13.81817	44.95136	2,767	53.58	1.21	15.38	9.78	0.15	8.27	9.74	2.51	0.08	0.07	100.8	106	0.089	23.1	184
AL4822-065	13.81794	44.95130	2,749	52.98	1.21	15.34	9.74	0.16	8.28	9.71	2.51	0.09	0.07	100.1	106	0.088	23.2	—
AL4822-066	13.81795	44.95130	2,749	52.90	1.21	15.29	9.81	0.16	8.29	9.76	2.50	0.08	0.08	100.1	106	0.089	23.2	48
AL4822-067	13.81636	44.94960	2,731	53.05	1.22	15.39	9.73	0.15	8.19	9.78	2.51	0.09	0.08	100.2	102	0.092	23.3	—

3.2. Crustal Magnetization

Near-bottom magnetic data acquired by *Sentry* provide insight into lithological variations across the 13°48'N OCC. High magnetization intensity is seen at the western edge of the *Sentry* survey, probably associated with a hanging wall composed of basaltic material (Figure 2c). Immediately east of the hanging-wall cutoff, magnetization is very low, consistent with a footwall composed of poorly magnetized crustal gabbro or mantle peridotite that has undergone low-temperature serpentinization (Klein et al., 2014; Sztikar & Dymont, 2014). A north-south oriented magnetization intensity high (~15 A/m) coincides with the series of domes at 44.95°W, flanked to the east by an area of low magnetization. This pattern of magnetization is consistent with a volcanic origin for the domes at the center of *Sentry* dive 374, with relatively poorly magnetized foot-wall material to the east and west.

3.3. Sediment Cover

Sediment thickness is a rough proxy for seafloor exposure time, assuming that sediment is delivered at a constant rate to the seafloor from the water column, and is not significantly disturbed post deposition by bottom currents. Assuming that sediments were uniformly deposited and undisturbed since emplacement, meter-scale variations in sediment thickness revealed in CHIRP data acquired by *Sentry* can be used to reconstruct the history of seafloor exposure by fault slip, volcanism, or erosion. This method has been used to demonstrate active slip on a detachment fault at 16°36'N on the MAR, since sediment progressively thickens on the footwall from 0 to ~2 m updip from the hanging-wall cutoff (Parnell-Turner et al., 2014).

CHIRP sub-bottom profiles reveal changes in the character and thickness of sediments overlying the detachment fault surface. Three discrete domains of sedimentary cover can be identified, consisting of the volcanic terrain and the footwall to the east and west, which can be distinguished based upon their thickness and acoustic character (Figure 3). In the western part of the exposed footwall, adjacent to the hanging-wall cutoff, the seabed reflection has moderate amplitude where sediment is present and is diffuse and low in amplitude where sediment is absent (e.g., Figures 4b and 4c). This weak character is probably due to uneven seafloor leading to scattering of energy and hence a diffuse reflection, which may arise due to local mass wasting and irregular sediment cover on this portion of the footwall. Sediment accumulations in this area are mostly acoustically transparent and lie above a basement that is marked by increased amplitude but lacks any coherent internal reflectivity. Sediment here is thin or absent, ranging in thickness from 0 to 3.8 m, with a mean of 1.3 ± 0.5 m (uncertainty is 1σ calculated from spot measurements spaced ~1 m apart along profiles in Figure 3).

In contrast, the volcanic terrain at the center of the survey is consistently blanketed by sediment 0.2–7.4 m thick, with a mean thickness of 3.3 ± 1.4 m (Figure 4i). The seafloor reflection on the volcanic terrain is bright in amplitude, and its attenuating character appears to cause the underlying reflections to have weaker amplitude. Nonetheless, a clear transition in reflectivity can be identified beneath the seabed, which is interpreted to represent the basement reflection, and can be mapped over most of the volcanic terrain (Figures 4j and 4k).

East of the volcanic terrain, a third domain is evident where the seafloor reflection is very bright in amplitude, which in most places obscures any reflectivity below (Figure 4d). This strong reflection indicates a sediment-water interface with greater acoustic impedance contrast, which could be explained by an increased degree of cementation and may explain its smooth appearance in the microbathymetry data. Where present, the basement reflection is relatively coherent and indicates a sediment thickness that varies from 0.2 to 9 m (Figure 4e), with a mean thickness of 4.1 ± 1.9 m.

3.4. Lithology and Geochemistry

The western part of the *Sentry* survey area is dominated by basalt boulders in a sedimented talus field below the main scarp of fault f2 (Figure 2a), based on the *Alvin* rock sampling. Samples AL4822-060 to AL4822-063 from this area are sparsely phyrlic basalts with rare rounded vesicles and devoid of glass. Samples AL4822-064 to AL4822-067 were collected on the volcanic terrain, composed of stacked pillows (and tentatively dikes), where individual basalt tubes and pillows protrude through the sediment cover above the scarp (Figure 5a). The suite of basalt samples is relatively fresh, with glass showing only moderate surface palagonite and most samples have a thin Mn-oxide coating. Samples AL4822-064 to AL4822-067 exhibit a narrow range in glass major element and volatile compositions (e.g., SiO₂ = 52.90–53.58 wt%; MgO = 8.19–8.28 wt%;

H₂O = 0.088–0.092 wt%; CO₂ = 102–106 ppm; Table 1). Vesicles are present in the outer quenched margin of each basalt sample collected from the volcanic terrain (example shown in Figure 5g), and the CO₂ released by crushing ranged from 48 to 183 ppm. The saturation pressure derived from the dissolved CO₂ and H₂O concentrations is ~5 MPa less than the collection pressure (equivalent to a depth of ~500 m with seawater density 1.027 g/cm³), based on VOLATILECALC and SolEX models (Dixon et al., 1995; Newman & Lowenstern, 2002; Witham et al., 2012). These solubility models are applicable for basalts with <52 wt% SiO₂, which is slightly exceeded in these samples. The solubility models presented by Ghiorso and Gualda (2015) and Papale et al. (2006) yield greater differences between the saturation pressure and collection pressure (>10 MPa). Although there are uncertainties associated with these solubility models due to the compositional extrapolation, these lavas are likely to be undersaturated in volatiles at their collection depth to some degree.

Samples AL4822-068 and AL4822-069 were collected updip of the volcanic terrain on the eastern footwall, from a hummocky outcrop of hydrothermally altered peridotite and trondhjemite, situated on a sedimented slope (Figures 5b–5f). In these samples, peridotite is completely altered to serpentine and magnetite with minor chlorite, while talc alteration is most pronounced on rock surfaces forming centimeter-sized coronas. In addition, talc penetrates the interior along monomineralic veins and occurs together with serpentine in bastite texture after orthopyroxene (Figures 5c and 5d). Shear phacoids, non-pseudomorph textures, and kinked veins indicate that tectonic movements postdate serpentinization and talc alteration. Trondhjemite from this outcrop consists of albitic plagioclase, quartz, chlorite, and anatase (Figures 5e and 5f). Plagioclase and quartz contain abundant fluid inclusions and amphibole, which is possibly altered to quartz and chlorite. Millimeter-sized crack-seal veins cutting across the trondhjemite are composed of coarse-grained, inclusion-free quartz that also reach adjacent serpentinite.

The single pushcore sample collected during *Alvin* dive 4822 (AL4822-PC07) was collected on the north-facing slope of the volcanic terrain near sample site AL4822-063 (Figure 2a). Penetrating 19 cm, this core consists of very fine grained mud devoid of any visible layering or grading and is black to tan in color, with a covering of black and white shells in the top ~5 cm. The location and shallow penetration of this core mean that it does not provide sufficient calibration for the CHIRP sediment images.

4. Discussion

4.1. Volcanism on Detachment Footwall

Imaging and sampling of in situ pillow basalts and observed high magnetization in near-bottom *Sentry* data indicate that bathymetric domes at the center of the survey area are volcanic in origin, apparently cross-cutting the detachment surface. The surficial volcanism does not preclude the presence of an underlying north-south trending normal fault as suggested by MacLeod et al. (2009) and may be responsible for the large scarp, f2. This fault may have begun as a magma-filled crack that propagated through the detachment footwall, and later fault activity may have offset volcanic outcrops leading to recent mass wasting. West of this volcanic terrain, corrugated bathymetry and shallow slopes suggest that an additional section of inactive detachment fault is exposed, bounded to the west by a well-defined hanging-wall cutoff (Figure 2).

Most mid-ocean ridge basalt samples display saturation pressures roughly equal to their collection pressures due to equilibrium degassing or saturation pressures greater than their collection pressures due to short timescales for magma ascent and emplacement relative to timescales for CO₂ diffusion into bubbles (Dixon et al., 1988). Some mid-ocean ridge basalt samples display saturation pressures less than their collection pressures and do not contain exsolved volatiles, probably because the magma never reached volatile saturation (e.g., Michael & Graham, 2015). Lavas collected from the 13°48'N OCC are unusual given that saturation pressures are less than the collection pressures despite the presence of exsolved volatiles (Figure 6). Based on VOLATILECALC and SolEX results, these saturation pressures are not highly sensitive to temperature, initial volatile concentrations, or degassing path (i.e., open versus closed system) (Dixon et al., 1995; Newman & Lowenstern, 2002; Witham et al., 2012). Interpretation of calculated saturation pressures relative to collection pressures assumes that solubility model uncertainties are <10% and that the high silica content (~53 wt%) relative to the model calibration (i.e., up to 49 wt%) does not affect H₂O and CO₂ solubility. Several hypotheses could explain the shallow saturation pressures relative to collection pressures (Figure 7) and the change in sediment thickness on either side of the volcanic terrain (Figure 3). Lavas could have been erupted at a shallower depth, equilibrated with that pressure, and then flowed downslope, or the magma feeding the

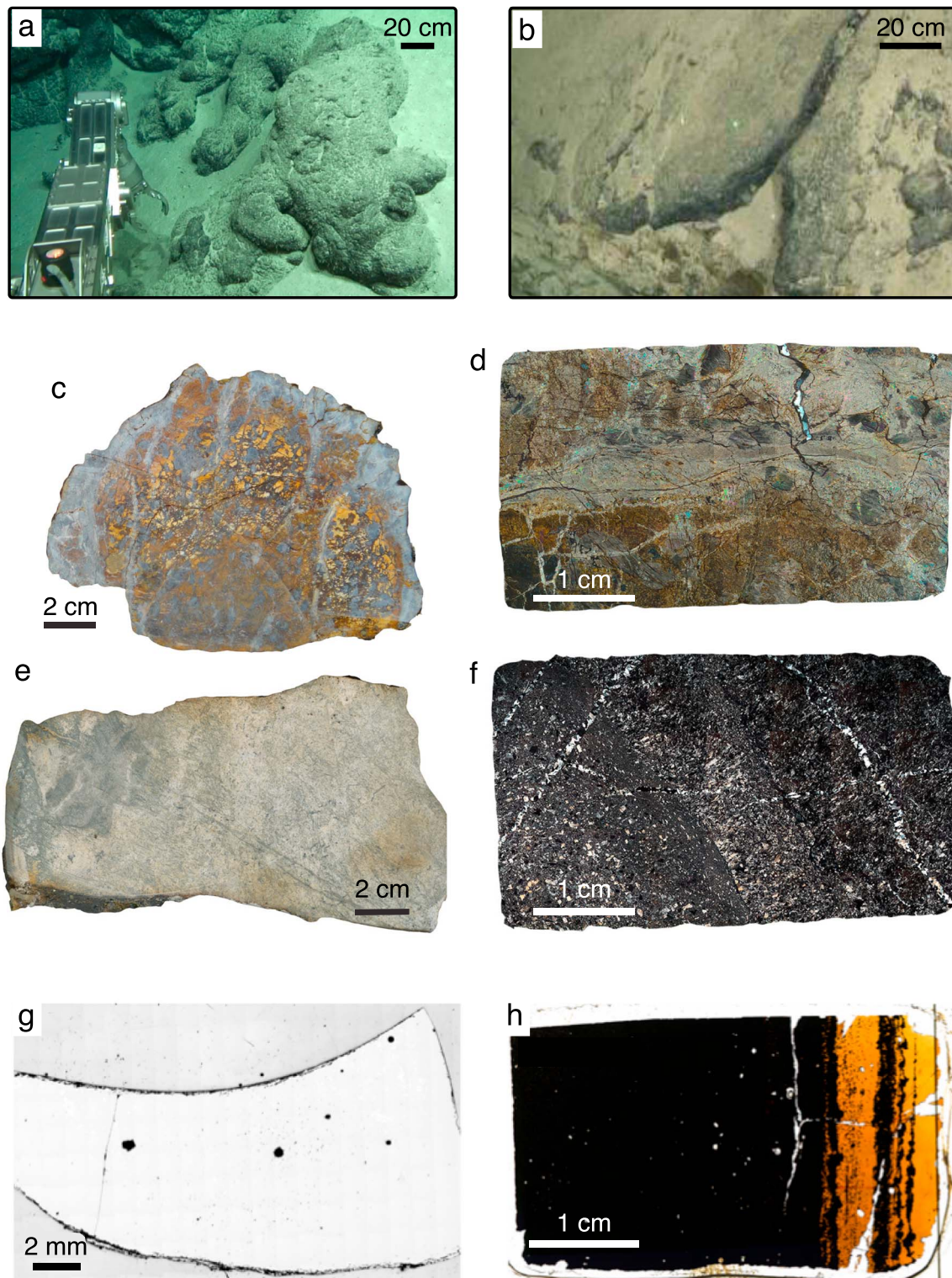


Figure 5. Outcrop photographs and rock samples from *Alvin* dive 4822. (a) Pillow basalt outcrop at site 67, located at top of volcanic terrain. (b) Serpentinized peridotite outcrop at site 68, located on eastern detachment footwall. (c) Serpentinized peridotite hand specimen, site 68. Sample underwent additional Si metasomatism and weathering, leading to formation of talc, quartz, hematite, and goethite. (d) Thin section photomicrograph mosaic in cross-polarized transmitted light of serpentinized peridotite, site 68. (e) Hydrothermally altered trondhjemite hand specimen, site 69, located on eastern detachment footwall. (f) Thin section photomicrograph mosaic in cross-polarized transmitted light of hydrothermally altered trondhjemite from site 69, consisting of albitic plagioclase, quartz, chlorite, and anatase. (g) Reflected light photomicrograph of the outer quenched margin of basalt sample 65. Dark gray is epoxy mount, light gray is basalt glass, and black dots are vesicles within glass. (h) Thin section photomicrograph in plane-polarized transmitted light of glassy basalt from site 64.

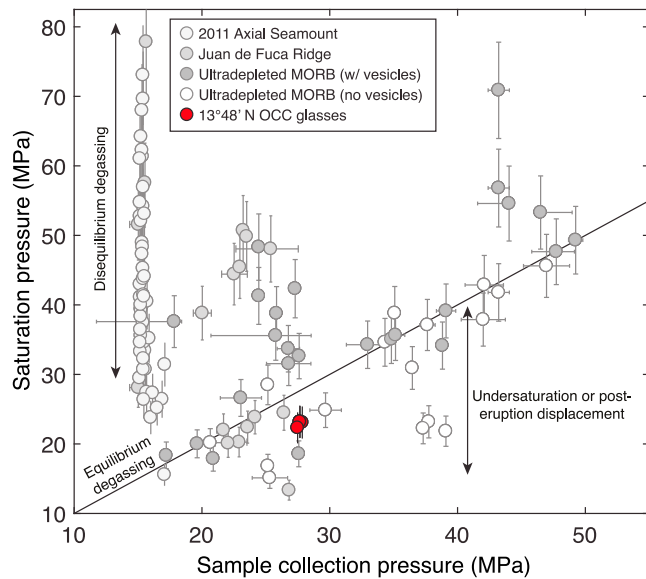


Figure 6. Saturation pressure versus sample collection pressure for pillow basalts collected from 13°48'N detachment footwall (red circles), compared to ultradepleted mid-ocean ridge basalt (MORB) samples from elsewhere. Gray shaded circles are samples containing vesicles, from global database (Michael & Graham, 2015), 2011 Axial Seamount eruption (Jones et al., 2018), and Juan de Fuca Ridge (Dixon et al., 1988); white circles are ultradepleted MORB that do not contain vesicles (Michael & Graham, 2015), which likely never reached volatile saturation; black line is 1:1 reference. Samples with vesicles lie mostly above 1:1 reference line, which represents equilibrium degassing due to rapid ascent and emplacement relative to CO₂ degassing timescale (Dixon et al., 1988). Samples from 13°48'N detachment footwall contain vesicles and are undersaturated, which could be explained by post-eruption vertical displacement. Saturation pressure error based on 10% uncertainty in CO₂ and H₂O; collection pressure error for dredged samples obtained from depth at start/end of dredge.

lava flows could have reached (and equilibrated at) a shallower depth during dike intrusion but erupted at their current position. Both of these hypotheses are implausible, however, given that the exsolved gas likely would have equilibrated with the melt at the present depth. Based on the volatile concentrations alone, the most likely scenario is that the lavas were emplaced ~500 m shallower than their present depth and subsequently downthrown on an updip fault. The only candidate fault near this scale is f1, which only has up to 200 m of vertical displacement but can be traced in towed sidescan data upslope of the volcanic deposit (Figure 1; MacLeod et al., 2009).

4.2. Timing of Volcanism and Fault Deactivation

Thin (1.3 ± 0.5 m) sediments over the western part of the detachment fault surface may indicate that little time has passed since its exposure for sediment to accumulate, consistent with earlier sidescan sonar observations (MacLeod et al., 2009). Since sediment covering the volcanic terrain to the east is thicker (3.3 ± 1.4 m) than that covering the western footwall, slip on the detachment fault may have continued after emplacement of the volcanic outcrop. In this interpretation, the ~2.5 km span of seafloor between the western edge of the volcanic terrain and the hanging-wall cutoff must have been exhumed in the period between volcanic emplacement and cessation of detachment slip (Figures 7b and 7c). Assuming 30% spreading asymmetry and a full spreading rate of 25.5 km/Ma (Mallows & Searle, 2012), we estimate that the fault continued to slip for ~150 ka after magmatic emplacement.

Piston cores located between 10° and 15°N on the MAR indicate that the sediment accumulation rate since Marine Isotope Stage 5 (130 ka) is 7 ± 2 mm/ka (Damuth, 1977). Hence, the 1.3 ± 0.5 m of sediment cover imaged on the western edge of the detachment footwall suggests that this fault surface has been inactive for 185 ± 89 ka. However, the potential effects of mass wasting in the area make this estimate uncertain.

Summing the final period of slip (~150 ka; see above) and period of fault inactivity gives an age of emplacement for the volcanic terrain of 335 ± 89 ka, which is broadly consistent with the observed 3.3 ± 1.4 m of sediment cover there, which would accumulate over an interval of 470 ± 123 ka. These age estimates are underconstrained due to the lack of a more accurate local sedimentation rate estimate; however, the observed relative differences in sediment thickness are robust if sedimentation rate has been constant over the past ~500 ka. The contrasting sediment cover across the volcanic terrain and western footwall provides evidence for detachment fault slip after emplacement of the volcanic terrain. This hypothesis, however, is not consistent with the undersaturated volatile content of basalts from the volcanic edifice.

A key assumption in the sediment accumulation proxy is that sediments observed over the western footwall retain their original, uniform depositional thickness and have not been significantly modified by mass wasting or erosion. *Alvin* dive video and sidescan sonar data indicate that sediments on the western footwall are covered in patchy rubble and talus (Figure 3), suggesting that basement material may have undergone mass wasting, in particular near steep scarps such as at fault f2 (Figure 2). These scarps and talus fields may have led to variations in initial sediment thickness, as fine-grained material may have ponded within local bathymetric hollows or adjacent to steep scarps (for an example of apparent ponding see Figure 4c).

We cannot rule out the possibility that sediment on the western footwall was originally of similar thickness to that on the volcanic terrain and has subsequently been eroded by mass wasting or redistributed by bottom currents. If the sediment on the western footwall and volcanic terrain were originally of equal thickness, then volcanic emplacement must have been contemporaneous with the cessation of detachment fault slip, and activity at the 13°48'N OCC must have ended at a similar time to the volcanism at 470 ± 123 ka. In this case, volcanic material probably breached the corrugated detachment surface at this time and erupted ~2.5 km

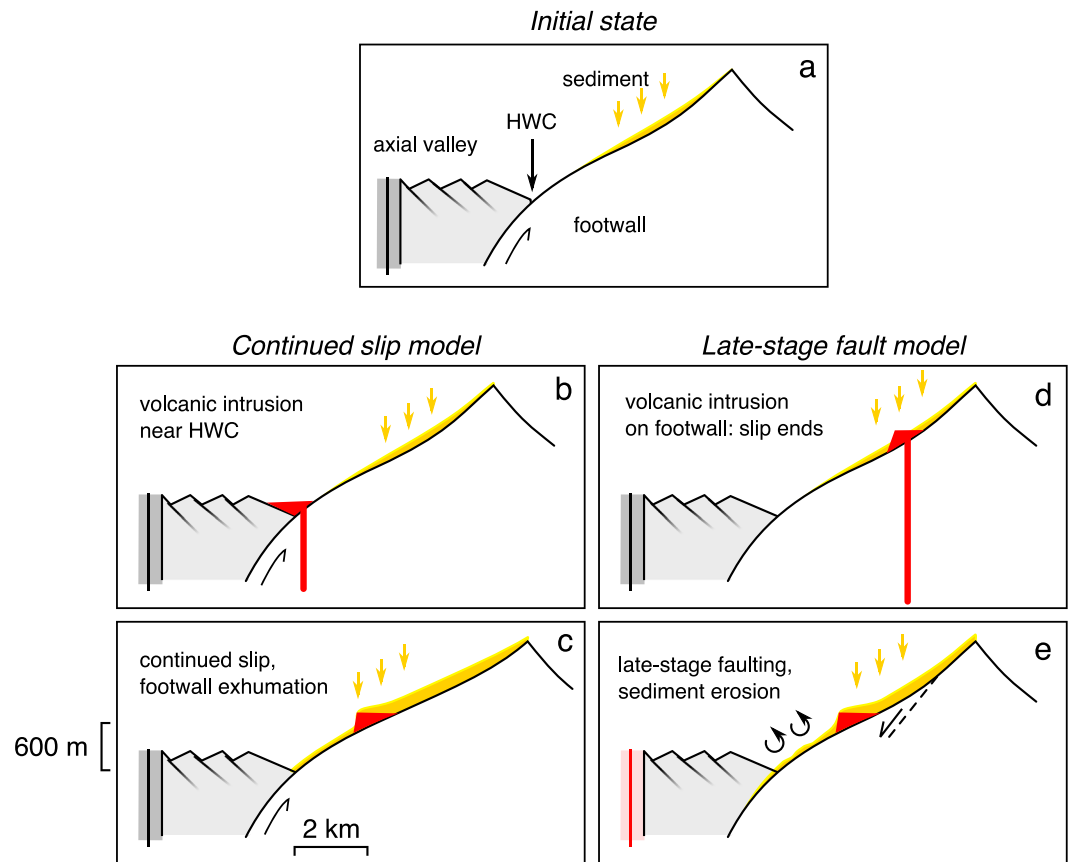


Figure 7. Cartoon illustrating hypotheses for near-bottom observations at 13°48'N detachment fault. (a) Initial state: Slip on detachment fault accommodates plate spreading prior to deactivation. Gray shaded block is hanging wall; HWC is hanging-wall cutoff; dark gray line is spreading axis; yellow arrows show sediment delivery from water column; yellow shading is sediment cover; black arrow shows slip direction. (b and c) Continued slip model: Volcanic intrusion (red line/shading) erupts near HWC, followed by continued slip that exposes further footwall on the seafloor. (d and e) Late-stage fault model: Volcanic intrusion on footwall, causing slip to cease; extension taken up by magmatism in axial valley (pink shading); sediment accumulated on footwall eroded and transported away by current activity (black arrows); volcanic material downthrown by fault (f1) on upper slope of footwall (dashed line).

east of the hanging-wall cutoff (Figure 7d). Post eruption, the volcanic edifice was downthrown by ~500 m by a fault, f1 (Figure 1), consistent with the observed lava volatile content (Figure 7e). Thin or absent sediments on the footwall west of the volcanic edifice are therefore explained by postdepositional mass wasting and transport, possibly by strong bottom currents within the axial valley (Figure 7e). In this interpretation, the back-tilt of the volcanic terrain (Figure 2b) would result from clockwise tilt as the volcanic material was downthrown toward the axis as a contiguous block after emplacement.

Deep-water flow speed measurements, experimental data, and theoretical arguments show that the onset of surface erosion of mud and silt is likely to occur at current velocities above 10–12 cm/s, while velocities of >30 cm/s are required to remove all but the sand fraction (Gross & Williams, 1991; McCave & Hall, 2006). Axis-parallel flow speeds measured in a similar settings on the MAR are much lower than these erosional thresholds, averaging 2 cm/s near 29°N (Murton et al., 1999), and 5–6 cm/s near the Rainbow hydrothermal vent field (German et al., 1998). Since direct observations of flow speed are not available near 13°48'N, vehicle dynamics from *Sentry* provide a qualitative way to estimate modern current strength during the dive. Figure S19 shows that *Sentry*'s heading closely matched the trackline heading throughout dive 374, both during east-west and north-south directions of travel. This observation suggests that there were no strong east-west or north-south flowing currents acting during the dive, although this finding does not rule out stronger currents in the past. Hence, on balance, we suggest that erosion of sediment may have been negligible in the region of the 13°48'N OCC footwall.

4.3. Mechanism for Halting Detachment Fault Slip

Seafloor observations at the nearby 13°30'N OCC show that the end of slip was probably caused by lateral propagation of neovolcanic ridges and dikes along strike within the axial valley, which cut across the emerging corrugated surfaces (MacLeod et al., 2009). At the toe of the 13°30'N OCC, chilled diabase dikes have also been mapped and sampled in the hanging wall above the detachment footwall and are interpreted to represent syn- or post-uplift magmatic intrusion (Bonnemains et al., 2017). A series of normal faults oriented perpendicular to corrugations have cut across the dome near the hanging-wall cutoff, three of which have propagated across the OCC tip to define a small local graben (Escartín et al., 2017). Elsewhere, at Integrated Ocean Drilling Program Hole U1309B on Atlantis Massif (also on the MAR), a series of sill-like bodies and diabase dikes were encountered, which are thought to have been emplaced during late stages of slip there (Blackman et al., 2011; Ildonse et al., 2007). Steeply dipping lithological contacts in Hole U1309D provide further evidence that late basaltic intrusions were intruded subparallel to the steep portion of the fault (McCaig et al., 2010).

Evidence for a punctuated sequence of slip, volcanism, and renewed slip can be found at other extinct detachments, for example, at Mount Dent on the Mid-Cayman Spreading Center. A low seismic velocity anomaly 5 km beneath the Mount Dent massif and Von Dam Vent Field can be explained either by reduced magmatism leading to a cracking front and deep fluid circulation or by intrusive magmatic sills (Harding et al., 2017). Although either hypothesis would lead to a cessation of slip and is equally valid, the link between changing magma supply and fault slip is comparable with observations at 13°48'N. At the nearby Mount Hudson OCC (also on the Mid-Cayman Spreading Center), the youngest portion of the detachment fault surface is cross-cut by an axial volcanic ridge, marked by a line of conical volcanic edifices (Cheadle et al., 2012; Hayman et al., 2011). The relative positions of the hanging-wall cutoff and volcanic terrains at Hudson Dome, and the 13°48'N OCC described here, are strikingly similar, suggesting a sequence of volcanic emplacement, short-lived fault slip, and final halting. Hence, in the later stages of OCC formation, increased magmatism may episodically bring lavas to the surface, perhaps following cracks and faults within the footwall. At 13°48'N and at Hudson Dome, this eruptive phase may have been followed by a brief period of detachment slip (on 100-ka timescale), prior to the final halting of slip altogether (Cheadle et al., 2012). This final phase of fault slip may come to an end once magma supply increased so that extension is preferentially taken up by expansion of magma-filled dikes within the axial valley. Finally, evidence of contemporaneous magmatism and fault slip is found at the 15°45'N OCC on the MAR, where undeformed diabase dikes with chilled margins cross-cut the corrugated detachment surface (Escartín et al., 2003). These dike intrusions are thought to have been restricted spatially and temporally, so that the detachment footwall may have continued to slip as a single cohesive unit, thus retaining mechanical integrity.

5. Conclusions

We have used near-bottom geophysical and lithological observations acquired by AUV and submersible dives at a domed core complex on the MAR to reconstruct the final stages of volcanism and faulting. Photographs and sampling of in situ basalt pillows and high magnetization recorded in near-bottom AUV data confirm that the 13°48'N OCC is cross-cut by an ~850 m-wide volcanic terrain, which also coincides with an axis-parallel normal fault. Bathymetric corrugations are observed east and west of this feature, while ultramafic lithologies have been sampled and drilled nearby, confirming the presence of an exhumed detachment footwall.

CHIRP sub-bottom profile images show that sediment thickness varies across the detachment fault system, which is used here as a rough proxy for seafloor exposure time. The saturation pressures from dissolved H₂O and CO₂ in vesicular lavas sampled on the footwall are less than the collection pressures, which could be explained by a depth increase since emplacement due to secondary faulting (Figures 7d and 7e). If sediments on the western footwall are undisturbed by mass wasting and redistribution by bottom currents, then the differences in sediment thickness imply that this section of the fault must have been exhumed after volcanic emplacement, implying that detachment fault activity continued for ~150 ka after volcanism. We favor this hypothesis since there is no evidence for the high flow speeds required to remove sediment from the western footwall, and it is consistent with evidence of slip after magmatism at OCCs elsewhere. Although the episode of magmatism must have been insufficient to immediately halt slip on the detachment fault, the association between changing magma supply and fault inactivity may apply to OCCs in general.

Acknowledgments

Data will be available online from the Marine Geoscience Data System (MGDS). We gratefully acknowledge the dedicated personnel associated with R/V *Atlantis*, AUV *Sentry*, and deep submergence vehicle *Alvin*, and the entire scientific party of the Popping Rocks cruise, AT33-03. We thank N. Hayman and an anonymous reviewer for their helpful comments. Seagoing and analytical efforts were supported by National Science Foundation grants OCE-1259218, OCE-1260578, and OCE-1736547.

References

- Blackman, D. K., Canales, J. P., & Harding, A. J. (2009). Geophysical signatures of oceanic core complexes. *Geophysical Journal International*, 178(2), 593–613. <https://doi.org/10.1111/j.1365-246X.2009.04184.x>
- Blackman, D. K., Cann, J. R., Janssen, B., & Smith, D. K. (1998). Origin of extensional core complexes: Evidence from the Mid-Atlantic Ridge at Atlantis Fracture Zone. *Journal of Geophysical Research*, 103(B9), 21,315–21,333. <https://doi.org/10.1029/98JB01756>
- Blackman, D. K., Ildefonse, B., John, B. E., Ohara, Y., Miller, D. J., Abe, N., et al. (2011). Drilling constraints on lithospheric accretion and evolution at Atlantis Massif, Mid-Atlantic Ridge 30°N. *Journal of Geophysical Research*, 116, B07103. <https://doi.org/10.1029/2010JB007931>
- Bonnemains, D., Escartin, J., Mével, C., Andreani, M., & Verlaquet, A. (2017). Pervasive silicification and hanging wall overplating along the 13°20'N oceanic detachment fault (Mid-Atlantic Ridge). *Geochemistry, Geophysics, Geosystems*, 18, 2028–2053. <https://doi.org/10.1002/2017GC006846>
- Buck, W. R., Lavier, L., & Poliakov, A. N. B. (2005). Modes of faulting at mid-ocean ridges. *Nature*, 434, 719–723. <https://doi.org/10.1038/nature03358>
- Cannat, M., Sauter, D., Mendel, V., Ruellan, E., Okino, K., Escartin, J., et al. (2006). Modes of seafloor generation at a melt-poor ultraslow-spreading ridge. *Geology*, 34(7), 605–608. <https://doi.org/10.1130/G22486.1>
- Caress, D. W., & Chayes, D. L. (1996). Improved processing of Hydrosweep DS multibeam data on the R/V *Maurice Ewing*. *Marine Geophysical Researches*, 18(6), 631–650. <https://doi.org/10.1007/BF00313878>
- Cheadle, M. J., John, B. E., German, C. R., & Kuszniir, N. J. (2012). The death throes of ocean core complexes: Examples from the Mid-Cayman Spreading Centre. *Abstract OS11E-01 Presented at 2012 Fall Meeting, AGU, San Francisco, Calif. 5-9 Dec.*
- Cohen, J. K., & Stockwell, J. W. (2013). CWP/SU: Seismic Un*x. *Release No. 43R5: an open source software package for seismic research and processing*. Center for Wave Phenomena, Colorado School of Mines.
- Coney, P. J. (1974). Structural analysis of the Snake Range "décollement," east-central Nevada. *Bulletin Geological Society of America*, 85(6), 973–978. [https://doi.org/10.1130/0016-7606\(1974\)85<973:SAOTSR>2.0.CO;2](https://doi.org/10.1130/0016-7606(1974)85<973:SAOTSR>2.0.CO;2)
- Coney, P. J., & Harms, T. A. (1984). Cordilleran metamorphic core complexes: Cenozoic extensional relics of Mesozoic compression. *Geology*, 12(9), 550–554. [https://doi.org/10.1130/0091-7613\(1984\)12<550:CMCCCE>2.0.CO;2](https://doi.org/10.1130/0091-7613(1984)12<550:CMCCCE>2.0.CO;2)
- Craig, T. J., & Parnell-Turner, R. (2017). Depth-varying seismogenesis on an oceanic detachment fault at 13°20'N on the Mid-Atlantic Ridge. *Earth and Planetary Science Letters*, 479, 60–70. <https://doi.org/10.1016/j.epsl.2017.09.020>
- Damuth, J. E. (1977). Late Quaternary sedimentation in the western equatorial Atlantic Late Quaternary sedimentation in the western equatorial Atlantic. *Geological Society of America Bulletin*, 88(5), 695–710. [https://doi.org/10.1130/0016-7606\(1977\)88<695:LQSIW>2.0.CO;2](https://doi.org/10.1130/0016-7606(1977)88<695:LQSIW>2.0.CO;2)
- Dick, H. J. B. (1989). Abyssal peridotites, very slow spreading ridges and ocean ridge magmatism. *Geological Society Special Publication*, 42(1), 71–105. <https://doi.org/10.1144/GSL.SP.1989.042.01.06>
- Dixon, J. E., Stolper, E. M., & Delaney, J. R. (1988). Infrared spectroscopic measurements of CO₂ and H₂O in Juan de Fuca Ridge basaltic glasses. *Earth and Planetary Science Letters*, 90(1), 87–104. [https://doi.org/10.1016/0012-821X\(88\)90114-8](https://doi.org/10.1016/0012-821X(88)90114-8)
- Dixon, J. E., Stolper, E. M., & Holloway, J. R. (1995). An experimental study of water and carbon dioxide solubilities in mid-ocean ridge basaltic liquids. Part II: Applications to degassing. *Journal of Petrology*, 36, 1607–1631. <https://doi.org/10.1093/oxfordjournals.petrology.a037268>
- Escartin, J., & Canales, J. P. (2011). Detachments in oceanic lithosphere: Deformation, magmatism, fluid flow, and ecosystems. *Eos, Transactions American Geophysical Union*, 92(4), 31.
- Escartin, J., Mével, C., MacLeod, C. J., & McCaig, A. M. (2003). Constraints on deformation conditions and the origin of oceanic detachments: The Mid-Atlantic Ridge core complex at 15°45'N. *Geochemistry, Geophysics, Geosystems*, 4(8), 1067. <https://doi.org/10.1029/2002GC000472>
- Escartin, J., Smith, D. K., Cann, J. R., Schouten, H., Langmuir, C. H., & Escrig, S. (2008). Central role of detachment faults in accretion of slow-spreading oceanic lithosphere. *Nature*, 455(7214), 790–794. <https://doi.org/10.1038/nature07333>
- Escartin, J., Smith, D. K., & Cannat, M. (2003). Parallel bands of seismicity at the Mid-Atlantic Ridge, 12–14°N. *Geophysical Research Letters*, 30(12), 1620. <https://doi.org/10.1029/2003GL017226>
- Escartin, J., Petersen, S., Bonnemains, D., Cannat, M., Andreani, M., Bezos, A., et al. (2017). Tectonic structure, evolution, and the nature of oceanic core complexes and their detachment fault zones (13°20' N and 13°30'N, Mid Atlantic Ridge). *Geochemistry, Geophysics, Geosystems*, 18, 1451–1482. <https://doi.org/10.1002/2016GC006775>
- German, C. R., Richards, K. J., Rudnicki, M. D., Lam, M. M., & Charlou, J.-L. (1998). Topographic control of a dispersing hydrothermal plume. *Earth and Planetary Science Letters*, 156(3–4), 267–273. [https://doi.org/10.1016/S0012-821X\(98\)00020-X](https://doi.org/10.1016/S0012-821X(98)00020-X)
- Ghiorso, M. S., & Gualda, G. A. R. (2015). An H₂O–CO₂ mixed fluid saturation model compatible with rhyolite-MELTS. *Contributions to Mineralogy and Petrology*, 169, 53. <https://doi.org/10.1007/s00410-015-1141-8>
- Gross, T. F., & Williams, A. J. (1991). Characterization of deep-sea storms. *Marine Geology*, 99(3–4), 281–301. [https://doi.org/10.1016/0025-3227\(91\)90045-6](https://doi.org/10.1016/0025-3227(91)90045-6)
- Guspi, F. (1987). Frequency-domain reduction of potential field measurements to a horizontal plane. *Geoexploration*, 24(2), 87–98. [https://doi.org/10.1016/0016-7142\(87\)90083-4](https://doi.org/10.1016/0016-7142(87)90083-4)
- Harding, J. L., Van Avendonk, H. J. A., Hayman, N., Grevemeyer, I., Peirce, C., & Dannowski, A. (2017). Magmatic-tectonic conditions for hydrothermal venting on an ultraslow-spread oceanic core complex. *Geology*, 45(9), 839–842. <https://doi.org/10.1130/G39045.1>
- Hauri, E., Wang, J., Dixon, J. E., King, P. L., Mandeville, C., & Newman, S. (2002). SIMS analysis of volatiles in silicate glasses. *Chemical Geology*, 183(1–4), 99–114. [https://doi.org/10.1016/S0009-2541\(01\)00375-8](https://doi.org/10.1016/S0009-2541(01)00375-8)
- Hayman, N., Grindlay, N., Perfit, M., Mann, P., Leroy, S., & De Lépinay, B. (2011). Oceanic core complex development at the ultraslow spreading Mid-Cayman Spreading Center. *Geochemistry, Geophysics, Geosystems*, 12, Q0AG02. <https://doi.org/10.1029/2010GC003240>
- Ildefonse, B., Blackman, D. K., John, B. E., Ohara, Y., Miller, D. J., & MacLeod, C. J. (2007). Oceanic core complexes and crustal accretion at slow-spreading ridges. *Geology*, 35(7), 623–626. <https://doi.org/10.1130/G23531A.1>
- Jones, M. R., Soule, S. A., Gonnermann, H. M., Le Roux, V., & Clague, D. A. (2018). Magma ascent and lava flow emplacement rates during the 2011 Axial Seamount eruption based on CO₂ degassing. *Earth and Planetary Science Letters*, 494, 32–41. <https://doi.org/10.1016/j.epsl.2018.04.044>
- Karson, J. A., & Dick, H. J. B. (1983). Tectonics of ridge-transform intersections at the Kane fracture zone. *Marine Geophysical Researches*, 6(1), 51–98. <https://doi.org/10.1007/BF00300398>
- Klein, F., Bach, W., Humphris, S. E., Kahl, W. A., Jöns, N., Moskowitz, B., & Berquó, T. S. (2014). Magnetite in seafloor serpentinite—Some like it hot. *Geology*, 42(2), 135–138. <https://doi.org/10.1130/G35068.1>
- Lister, G. S., & Davis, G. A. (1989). The origin of metamorphic core complexes and detachment faults formed during Tertiary continental extension in the northern Colorado River region, USA. *Journal of Structural Geology*, 11(1–2), 65–94. [https://doi.org/10.1016/0191-8141\(89\)90036-9](https://doi.org/10.1016/0191-8141(89)90036-9)

- MacLeod, C. J., Searle, R. C., Murton, B. J., Casey, J. F., Mallows, C., Unsworth, S. C., et al. (2009). Life cycle of oceanic core complexes. *Earth and Planetary Science Letters*, 287(3–4), 333–344. <https://doi.org/10.1016/j.epsl.2009.08.016>
- Mallows, C., & Searle, R. C. (2012). A geophysical study of oceanic core complexes and surrounding terrain, Mid-Atlantic Ridge 13°N–14°N. *Geochemistry, Geophysics, Geosystems*, 13, Q0AG08. <https://doi.org/10.1130/G39232.1>
- McCaug, A. M., Delacour, A., Fallick, A. E., Castelain, T., & Früh-Green, G. L. (2010). Detachment fault control on hydrothermal circulation systems: Interpreting the subsurface beneath the TAG hydrothermal field using the isotopic and geological evolution of oceanic core complexes in the Atlantic. In P. A. Rona, C. W. Devey, & B. J. Murton (Eds.), *Diversity of hydrothermal systems on slow spreading ocean ridges*, (pp. 207–239). Washington, D. C.: American Geophysical Union. doi:<https://doi.org/10.1029/2008GM000729>
- McCave, I. N., & Hall, I. R. (2006). Size sorting in marine muds: Processes, pitfalls, and prospects for paleoflow-speed proxies. *Geochemistry, Geophysics, Geosystems*, 7, Q10N05. <https://doi.org/10.1029/2006GC001284>
- Michael, P. J., & Graham, D. W. (2015). The behavior and concentration of CO₂ in the suboceanic mantle: Inferences from undegassed ocean ridge and ocean island basalts. *Lithos*, 236–237, 338–351. <https://doi.org/10.1016/j.lithos.2015.08.020>
- Murton, B. J., Redbourn, L. J., German, C. R., & Baker, E. T. (1999). Sources and fluxes of hydrothermal heat, chemicals and biology within a segment of the Mid-Atlantic Ridge. *Earth and Planetary Science Letters*, 171(2), 301–317. [https://doi.org/10.1016/S0012-821X\(99\)00157-0](https://doi.org/10.1016/S0012-821X(99)00157-0)
- Newman, S., & Lowenstern, J. B. (2002). VOLATILECALC: A silicate melt–H₂O–CO₂ solution model written in Visual Basic for Excel. *Computers & Geosciences*, 28(5), 597–604. [https://doi.org/10.1016/S0098-3004\(01\)00081-4](https://doi.org/10.1016/S0098-3004(01)00081-4)
- Ohara, Y., Yoshida, T., & Kasuga, S. (2001). Giant megamullion in the Parece Vela Backarc Basin. *Marine Geophysical Researches*, 22(1), 47–61. <https://doi.org/10.1023/A:1004818225642>
- Okino, K., Matsuda, K., Christie, D. M., Nogi, Y., & Koizumi, K. (2004). Development of oceanic detachment and asymmetric spreading at the Australian–Antarctic discordance. *Geochemistry, Geophysics, Geosystems*, 5, Q12012. <https://doi.org/10.1029/2004GC000793>
- Olive, J. A., Behn, M. D., & Tucholke, B. E. (2010). The structure of oceanic core complexes controlled by the depth distribution of magma emplacement. *Nature Geoscience*, 3(7), 491–495. <https://doi.org/10.1038/ngeo888>
- Parker, R. L., & Huestis, S. (1974). The inversion of magnetic anomalies in the presence of topography. *Journal of Geophysical Research*, 79(11), 1587–1593. <https://doi.org/10.1029/JB079i011p01587>
- Parnell-Turner, R., Cann, J. R., Smith, D. K., Schouten, H., Yoerger, D., Palmiotto, C., et al. (2014). Sedimentation rates test models of oceanic detachment faulting. *Geophysical Research Letters*, 41, 7080–7088. <https://doi.org/10.1002/2014GL061555>
- Parnell-Turner, R., Sohn, R. A., Peirce, C., Reston, T. J., Macleod, C. J., Searle, R. C., & Simão, N. (2017). Oceanic detachment faults generate compression in extension. *Geology*, 45(10), 923–926. <https://doi.org/10.1130/G39232.1>
- Smith, D. K., Cann, J. R., & Escartin, J. (2006). Widespread active detachment faulting and core complex formation near 13°N on the Mid-Atlantic Ridge. *Nature*, 442, 440–443. doi:<https://doi.org/10.1038/nature04950>, 7101
- Smith, D. K., Escartin, J., Cannat, M., Tolstoy, M., Fox, C. G., Bohnenstiehl, D. R., & Bazin, S. (2003). Spatial and temporal distribution of seismicity along the northern Mid-Atlantic Ridge (15°–35°N). *Journal of Geophysical Research*, 108(B3), 2167. <https://doi.org/10.1029/2002JB001964>
- Smith, D. K., Escartin, J., Schouten, H., & Cann, J. R. (2008). Fault rotation and core complex formation: Significant processes in seafloor formation at slow-spreading mid-ocean ridges (Mid-Atlantic Ridge, 13°–15°N). *Geochemistry, Geophysics, Geosystems*, 9, Q03003. <https://doi.org/10.1029/2007GC001699>
- Szitkar, F., & Dymant, J. (2014). Near-seafloor magnetics reveal tectonic rotation and deep structure at the TAG (Trans-Atlantic Geotraverse) hydrothermal site (Mid-Atlantic Ridge, 26°N). *Geology*, 43(1), 87–90. <https://doi.org/10.1130/G36086.1>
- Tian, X., & Choi, E. (2016). Effects of axially variable diking rates on faulting at slow spreading mid-ocean ridges. *Earth and Planetary Science Letters*, 458, 14–21. <https://doi.org/10.1016/j.epsl.2016.10.033>
- Tivey, M. A., Rona, P. A., & Schouten, H. (1993). Reduced crustal magnetization beneath the active sulfide mound, TAG hydrothermal field. *Earth and Planetary Science Letters*, 115(1–4), 101–115. [https://doi.org/10.1016/0012-821X\(93\)90216-V](https://doi.org/10.1016/0012-821X(93)90216-V)
- Tucholke, B. E., Behn, M. D., Buck, W. R., & Lin, J. (2008). Role of melt supply in oceanic detachment faulting and formation of megamullions. *Geology*, 36(6), 455. <https://doi.org/10.1130/G24639A.1>
- Tucholke, B. E., & Lin, J. (1994). A geological model for the structure of ridge segments in slow spreading ocean crust. *Journal of Geophysical Research*, 99(B6), 11,937–11,958. <https://doi.org/10.1029/94JB00338>
- Tucholke, B. E., Lin, J., & Kleinrock, M. C. C. (1998). Megamullions and mullion structure defining oceanic metamorphic core complexes on the Mid-Atlantic Ridge. *Journal of Geophysical Research*, 103(B5), 9857–9866. <https://doi.org/10.1029/98JB00167>
- Witham, F., Blundy, J., Kohn, S. C., Lesne, P., Dixon, J., Churakov, S. V., & Botcharnikov, R. (2012). SolEx: A model for mixed COHSCI-volatile solubilities and exsolved gas compositions in basalt. *Computers and Geosciences*, 45, 87–97. <https://doi.org/10.1016/j.cageo.2011.09.021>